Received: 29 January 2021 | Revised: 6 March 2021 | Accepted: 21 March 2021

DOI: 10.1002/htj.22142

RESEARCH ARTICLE

HEAT TRANSFER WILEY

Effects of multislip and distinct heat source on MHD Carreau nanofluid flow past an elongating cylinder using the statistical method

Alappat Sunny Sabu | **Sujesh Areekara** | **Alphonsa Mathew**

Department of Mathematics, St. Thomas' College (Autonomous), Thrissur, Kerala, India

Correspondence
Alphonsa Mathew, Department of Mathematics, St. Thomas' College (Autonomous), Thrissur, 680001 Kerala, India.
Email: alphonsa@stthomas.ac.in

Abstract

This study focuses on studying the impact of multiple slip effects on the hydromagnetic Carreau nanofluid flow over an elongating cylinder considering a linear heat source and exponential space-based heat source. Suitable transformations are used in converting the highly nonlinear system of partial differential equations governing the flow into a system of ordinary differential equations and hence resolved using the Runge–Kutta method of order four coupled with the shooting method. BVP5C and RKF45 are used to compare the numerical accuracy and an excellent agreement is noted. The parallel effect of parameters on Nusselt number is studied using surface plots and the corresponding effects are scrutinized using multiple linear regression. It is observed that the linear heat source parameter, thermal slip parameter and exponential space-based heat source parameter demote the heat transfer rate. The consequence of different parameters on drag coefficient and mass transfer are quantified using a linear regression slope.

KEYWORDS

Carreau nanofluid, exponential space-based heat source, MHD convective flow, multiple slip effect, regression analysis, stretching cylinder

1 | INTRODUCTION

Viscous fluid flow over an expanding cylinder has important applications in industry and engineering fields. Production of plastic films, rubber, copper wires, and paper are some industrial applications of viscous fluid flows. The heat transfer rate and stretching determine the quality and finishing of a product. Nanofluid flow over a lengthening cylinder with shape factor is considered in the study of Shaiq et al.[1] Heat transfer via a stretched cylinder utilizing nanofluids is important in food processing, glass fiber production, and metal spinning. Shojaei et al.[2] analyzed second-grade non-Newtonian fluid flow over a stretched cylinder and observed an elevated temperature profile due to large curvature parameter values. Hussain et al.[3] conducted a simultaneous study on the nanofluid flow over an elongating cylinder and a flat sheet. They noticed an increase in the velocity profile due to flow over a flat sheet when collated with flow over an expanding cylinder.

Buongiorno presented a new model based on the seven slip mechanism to covers all aspects of nanofluids among which thermophoresis and Brownian motion are highly regarded. Nanofluid flow over various attributes utilizing the Buongiorno model can be found in De,[4] Reddy et al.,[5] De,[6] Roşca et al.,[7] and De and Gorji.[8] Zeeshan et al.[9] presented magnetohydrodynamic (MHD) flow over a stretched cylinder using Buongiorno's model and observed that the concentration profile declined due to Brownian motion.

Fluids are categorized into two groups: Newtonian and non-Newtonian. A linear stress-strain relationship is observed in the case of Newtonian fluids. Paint, toothpaste, and honey do not obey such a relationship. The Carreau nanofluid model includes low and high shear rates, which is an attractive aspect in non-Newtonian studies. It is used to represent many manufacturing and chemical engineering flows. Eid et al.[10] studied Carreau nanofluid flow on top of an expanding sheet and found that the power-law index promotes velocity. The Carreau fluid flow on top of an elongating cylinder was numerically investigated by Khan et al.[11] They noticed a reverse relationship in the drag force due to the Weissenberg number. Salahuddin et al.[12] analyzed the slip effects of Carreau nanofluid over an elongated cylinder and observed a high-velocity profile for dilatant fluid due to augmentation in Weissenberg number.

The magnetic field induces a change in the nanofluid behavior, which has a vital role in engineering, industrial, and medical fields. Magnetometers, MHD throttles, plasma studies, glass fibers, and hot rolling, and so forth, are some examples where MHD flow is exploited. Gholinia et al.[13] studied the influence of magnetic field over an expanding cylinder utilizing carbon nanotube (CNT) nanofluids. With an increasing magnetic field parameter, a decrease in the surface drag was observed. Bilal et al.[14] numerically examined the MHD flow over a lengthening cylinder on Williamson fluid and noticed a decline in velocity profile due to an augmentation in magnetic field parameter. Sohail and Naz[15] incorporated a revised mass and heat transmission model in MHD flow over a stretched cylinder and attained the numerical solutions using the optimal homotopy asymptotic method.

Slip flow plays a significant role in the engineering and medical field. Microvalves, hard disk drives, internal cavities, and nozzles are a few examples where slip flow is utilized. Vinita and Poply[16] studied slip flow past a stretched cylinder and found a reduced velocity profile due to the slip parameter. Non-Newtonian and Newtonian fluids with slip effects are reviewed by numerous researchers. Effect of thermal slip and velocity slip past a stretching cylinder is found in Ogunseye et al.,[17] Mishra and Kumar,[18] and Usman et al.[19]

The heat source/sink parameter has a key role in the medical and industrial fields. Heat pumps, heat exchangers, and filtration device are a few examples exploiting the effect of various

heat sources. Nanofluid flow over an elongating cylinder with heat source is reviewed in Ahmed et al.[20] and Ali et al.[21] Gireesha et al.[22] studied CNT nanofluid flow on top of a curved elongating sheet and noticed an increase in temperature due to exponential space-based heat source (ESHS). Mahanthesh et al.[23] scrutinized the simultaneous effect of ESHS and linear heat source (LHS) parameter on the nanofluid flow over a stretchable rotating disk. They discovered an elevated heat transfer rate due to the ESHS parameter rather than the LHS parameter. Non-Newtonian and Newtonian fluid flow considering ESHS for different scenarios are studied by Mahanthesh et al.[24] and Nagaraja and Gireesha.[25]

However, Carreau nanofluid fluid flow over an elongating cylinder with multiple slip effects has not been investigated to date. ESHS and LHS effects are incorporated in the current study. Numerical solutions of the problem are obtained by transforming the system of partial differential equations (PDEs) into a system of ordinary differential equations (ODEs) and hence solving the transformed system using Runge–Kutta of fourth-order (RK4) coupled with shooting. To boost the novelty of the current study, the consequence of various parameters on heat transfer rate for pseudo-plastic and dilatant fluids are inspected using multiple linear regression (see Mahanthesh et al.,[26] Sabu et al.,[27] Mackolil and Mahanthesh,[28] Sabu et al.,[29] & Mackolil and Mahanthesh[30]). Furthermore, the response of different parameters on drag coefficient and mass transfer is quantified using the slope of linear regression via data points (see Mahanthesh et al.[24]).

2 | MATHEMATICAL FRAMEWORK

A steady, incompressible two-dimensional flow of an electrically conducting Carreau nanofluid over an elongating cylinder with radius $r = R$ is considered. A uniform magnetic field (of strength B_0) is administered along the r direction. Let the cylinder be fixed at origin O and stretched with a velocity $\frac{ax}{l}$ along the x direction (see Figure 1). Simultaneous effects of LHS and ESHS are considered. C_w and T_w are the constant values of concentration and temperature at the stretching cylinder, whereas the ambient values are denoted by T_∞ and C_∞ with r tending to infinity.

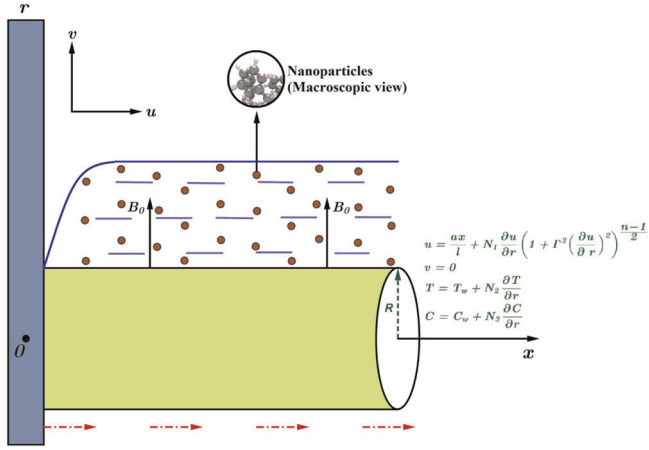

FIGURE 1 Figurative representation [Color figure can be viewed at wileyonlinelibrary.com]

The governing equations take the form (see Khan et al.[31]):

$$\frac{\partial}{\partial x}(ru)+\frac{\partial}{\partial r}(rv)=0, \tag{1}$$

$$u\frac{\partial u}{\partial x}+v\frac{\partial u}{\partial r}=\frac{\nu_f}{r}\frac{\partial u}{\partial r}\left(1+\Gamma^2\left(\frac{\partial u}{\partial r}\right)^2\right)^{\frac{n-1}{2}}+\nu_f\frac{\partial^2 u}{\partial r^2}\left(1+\Gamma^2\left(\frac{\partial u}{\partial r}\right)^2\right)^{\frac{n-1}{2}}$$
$$+\nu_f(n-1)\Gamma^2\left(\frac{\partial u}{\partial r}\right)^2\frac{\partial^2 u}{\partial r^2}\left(1+\Gamma^2\left(\frac{\partial u}{\partial r}\right)^2\right)^{\frac{n-3}{2}}-\frac{\sigma_f B_0^2 u}{\rho_f}, \tag{2}$$

$$u\frac{\partial T}{\partial x}+v\frac{\partial T}{\partial r}=\alpha_f\left(\frac{\partial^2 T}{\partial r^2}+\frac{1}{r}\frac{\partial T}{\partial r}\right)+\frac{(\rho C)_p}{(\rho C)_f}\left(D_B\frac{\partial C}{\partial r}\frac{\partial T}{\partial r}+\frac{D_T}{T_\infty}\left(\frac{\partial T}{\partial r}\right)^2\right)+\frac{q_T}{(\rho C)_f}(T-T_\infty)$$
$$+\frac{q_E}{(\rho C)_f}(T_w-T_\infty)e^{\frac{-m(r^2-R^2)}{2R}\sqrt{\frac{a}{l\nu_f}}}, \tag{3}$$

$$u\frac{\partial C}{\partial x}+v\frac{\partial C}{\partial r}=D_B\left(\frac{\partial^2 C}{\partial r^2}+\frac{1}{r}\frac{\partial C}{\partial r}\right)+\frac{D_T}{T_\infty}\left(\frac{\partial^2 T}{\partial r^2}+\frac{1}{r}\frac{\partial T}{\partial r}\right), \tag{4}$$

with

$$\left.\begin{aligned} u&=\tfrac{ax}{l}+N_1\tfrac{\partial u}{\partial r}\left(1+\Gamma^2\left(\tfrac{\partial u}{\partial r}\right)^2\right)^{\frac{n-1}{2}},\ v=0,\\ T&=T_w+N_2\tfrac{\partial T}{\partial r},\ C=C_w+N_3\tfrac{\partial C}{\partial r}\ \text{when } r=R\\ u&\to 0,\ T\to T_\infty,\ C\to C_\infty\ \text{when } r\to\infty \end{aligned}\right\}. \tag{5}$$

The following similarity variables (Salahuddin et al.[12]) are implemented in converting the above system of PDEs into a system of ODEs:

$$\left.\begin{aligned} u&=\tfrac{1}{r}\tfrac{\partial\psi}{\partial r},\ v=\tfrac{-1}{r}\tfrac{\partial\psi}{\partial x},\ \psi=\sqrt{\tfrac{a\nu_f}{l}}xRf(\zeta),\\ \zeta&=\left(\tfrac{r^2-R^2}{2R}\right)\sqrt{\tfrac{a}{l\nu_f}},\ \theta=\tfrac{T-T_\infty}{T_w-T_\infty},\ \phi=\tfrac{C-C_\infty}{C_w-C_\infty} \end{aligned}\right\}. \tag{6}$$

The transformed equations are as follows:

$$ff''+(n-1)We^2K(f'')^3(1+We^2(f'')^2)^{\frac{n-3}{2}}$$
$$+2Kf''(1+We^2(f'')^2)^{\frac{n-1}{2}}-Mf'-(f')^2$$
$$+(1+2K\zeta)f'''(1+We^2(f'')^2)^{\frac{n-1}{2}}$$
$$+(n-1)We^2(1+2K\zeta)(f'')^2f'''(1+We^2(f'')^2)^{\frac{n-3}{2}}=0, \tag{7}$$

$$(1+2K\zeta)\theta''+2K\theta'+Prf\theta'+Pr(1+2K\zeta)[Nb\phi'\theta'$$
$$+Nt(\theta')^2]+PrQ_T\theta+PrQ_Ee^{-m\zeta}=0, \tag{8}$$

$$(1+2K\zeta)\phi''+\frac{Nt}{Nb}(1+2K\zeta)\theta''+2K\left[\phi'+\frac{Nt}{Nb}\theta'\right]+Scf\phi'=0, \tag{9}$$

with

$$\left.\begin{aligned} f(0)=0, f'(0)=1+b_1 f''(0)\left[1+We^2 f''(0)^2\right]^{\frac{n-1}{2}}, \theta(0)=1+b_2\theta'(0), \\ \phi(0)=1+b_3\phi'(0), f'(\infty)\to 0, \theta(\infty)\to 0, \phi(\infty)\to 0 \end{aligned}\right\}, \tag{10}$$

where the nondimensional parameters are taken as follows:

$$\left.\begin{aligned} We^2=\frac{\Gamma^2 a^3 x^2 r^2}{\nu_f l^3 R^2}, K=\frac{1}{R}\sqrt{\frac{\nu_f l}{a}}, Sc=\frac{\nu_f}{D_B}, M=\frac{\sigma_f B_0^2 l}{a\rho_f}, Pr=\frac{\nu_f}{\alpha_f}, \\ Nb=\frac{(\rho C)_p D_B(C_w-C_\infty)}{\nu_f(\rho C)_f}, Nt=\frac{(\rho C)_p D_T(T_w-T_\infty)}{T_\infty \nu_f(\rho C)_f}, Q_T=\frac{q_T l}{a(\rho C)_f}, Q_E=\frac{q_E l}{a(\rho C)_f} \end{aligned}\right\}.$$

Drag coefficient (Cf), mass transfer rate (Sh), and heat transfer rate (Nu) are defined as follows (see Khan et al.[31]):

$$Cf=\frac{\tau_{rx}}{\frac{1}{2}\rho_f\left(\frac{ax}{l}\right)^2}, Sh=\frac{xq_m}{D_B(C_w-C_\infty)}, Nu=\frac{xq_w}{k_f(T_w-T_\infty)},$$

where

$$\tau_{rx}=\left(\mu_f\left(\frac{\partial u}{\partial r}\right)\left[1+\Gamma^2\left(\frac{\partial u}{\partial r}\right)^2\right]^{\frac{n-1}{2}}\right)_{r=R}, q_m=-D_B\left(\frac{\partial C}{\partial r}\right)_{r=R}, q_w=-k_f\left(\frac{\partial T}{\partial r}\right)_{r=R}.$$

The reduced physical quantities (using Equation 6) take the form:

$$\frac{Cf\,(Re_x)^{\frac{1}{2}}}{2}=f''(0)(1+We^2(f''(0))^2)^{\frac{n-1}{2}}, Sh\,(Re_x)^{-\left(\frac{1}{2}\right)}=-\phi'(0), Nu\,(Re_x)^{-\left(\frac{1}{2}\right)}=-\theta'(0).$$

3 | NUMERICAL SOLUTION

The highly nonlinear coupled ODEs (7)–(9) with the corresponding boundary conditions (10) are solved by engaging Runge–Kutta method of fourth-order together with the shooting technique with an accuracy of 10^{-6}. For the numerical computation, we have restricted infinity to 15 and a step size of 0.1 is chosen. The accuracy of the numerical method is guaranteed by performing a restrictive study with the already published results of Khan and Pop[32] and an excellent agreement (discussed in Table 1) is noted. Additionally, the numerical values computed using RK4 is compared with BVP5C and RKF45, which are presented in Table 2 and four-digit accuracy is obtained.

TABLE 1 Comparison of $Nu\,(Re_x)^{\frac{-1}{2}}$ with $We = K = M = Q_T = Q_E = Nt = b_1 = b_2 = b_3 = 0$ and $Nb \to 0$

	$Nu\,(Re_x)^{-\frac{1}{2}}$	
Pr	**Khan and Pop[32]**	**RK4**
0.7	0.4539	0.453932
2	0.9113	0.911359
7	1.8954	1.895428
20	3.3539	3.354174

TABLE 2 Comparison of $-\frac{1}{2}Cf\,(Re_x)^{\frac{1}{2}}$ with $M = Q_T = Q_E = Nt = b_1 = b_2 = b_3 = 0$ and $Nb \to 0$

			$-\frac{1}{2}Cf\,(Re_x)^{\frac{1}{2}}$		
n	**We**	**K**	**BVP5C**	**RKF45**	**RK4**
0.5	1	0.2	0.989702	0.989709	0.989709
	1	0.4	1.039950	1.039965	1.039965
	1	0.6	1.088334	1.088361	1.088361
	2	0.2	0.867191	0.867198	0.867198
	2	0.4	0.901331	0.901343	0.901343
	2	0.6	0.934526	0.934545	0.934545
	3	0.2	0.777193	0.777201	0.777201
	3	0.4	0.804360	0.804374	0.804374
	3	0.6	0.830948	0.830972	0.830972
1.5	1	0.2	1.145708	1.145708	1.145708
	1	0.4	1.239624	1.239625	1.239625
	1	0.6	1.332933	1.332936	1.332936
	2	0.2	1.247964	1.247965	1.247965
	2	0.4	1.367059	1.367061	1.367061
	2	0.6	1.485123	1.485127	1.485127
	3	0.2	1.335538	1.335539	1.335539
	3	0.4	1.474373	1.474375	1.474375
	3	0.6	1.611580	1.611585	1.611585

To accomplish this, we assume:

$$f = h_1, f' = h_2, f'' = h_3, \theta = h_4, \theta' = h_5, \phi = h_6, \phi' = h_7.$$

Accordingly, Equations (7)–(10) take the form:

$$h_1'' = h_2, h_2'' = h_3,$$

$$h_3' = \frac{-2Kh_3\left(1 + We^2h_3^2\right)^{\frac{n-1}{2}} - (n-1)We^2Kh_3^3\left(1 + We^2h_3^2\right)^{\frac{n-3}{2}} + Mh_2 + h_2^2 - h_1h_3}{\left[(1 + 2K\zeta)\left(1 + We^2h_3^2\right)^{\frac{n-1}{2}} + (n-1)We^2(1 + 2K\zeta)h_3^2\left(1 + We^2h_3^2\right)^{\frac{n-3}{2}}\right]},$$

$$h_4'' = h_5,$$

$$h_5' = \frac{-2Kh_5 - Prh_1h_5 - Pr(1 + 2K\zeta)\left[Nbh_5h_7 + Nth_5^2\right] - PrQ_Th_4 - PrQ_Ee^{-m\zeta}}{1 + 2K\zeta},$$

$$h_6'' = h_7,$$

$$h_7' = \frac{-\frac{Nt}{Nb}(1 + 2K\zeta)h_5' - 2K\left[h_7 + \frac{Nt}{Nb}h_5\right] - Sch_1h_7}{1 + 2K\zeta}.$$

The following initial conditions are considered:

$$h_1(0) = 0, h_2(0) = 1 + b_1s_1\left[1 + We^2{s_1}^2\right]^{\frac{n-1}{2}}, h_3(0) = s_1,$$

$$h_4(0) = 1 + b_2s_2, h_5(0) = s_2, h_6(0) = 1 + b_3s_3, h_7(0) = s_3,$$

where s_1, s_2, s_3 are unknowns and are found using the Newton–Raphson method with a suitable initial guess.

4 | RESULT AND DISCUSSION

The impact of velocity slip (b_1), thermal slip (b_2), concentration slip (b_3), Weissenberg number (We), linear heat source parameter (Q_T), thermophoresis parameter (Nt), Hartmann number (M), exponential heat source parameter (Q_E), curvature parameter (K), Brownian motion parameter (Nb) on concentration ($\phi(\zeta)$), temperature ($\theta(\zeta)$), and velocity ($f''(\zeta)$) profiles are carefully studied through Figures 2–13. The Schmidt number (Sc) and Prandtl number (Pr) are fixed at 1 and 3, respectively.

The discrepancy in $f''(\zeta)$ due to an increase in b_1 is depicted in Figure 2. Augmentation in b_1 shows a reduction in $f''(\zeta)$ for both dilatant and pseudo-plastic fluids. Mounting values of b_1 causes a reduction in the movement of fluid particles and hence $f''(\zeta)$ decreases. Figure 3 delineates the decrease in $\theta(\zeta)$ with increasing b_2 values. Physically, augmenting the thermal slip parameter minimizes the sensitivity of the fluid flow within the boundary layer, which diminishes the amount of heat produced and thus reduces the temperature. It is further noted that the thermal boundary layer thickness of pseudo-plastic fluid is greater than dilatant fluid.

Figure 4 depicts the variation of $f''(\zeta)$ due to the enhancement in M. An augmentation in M produces the Lorentz force, and hence a resistance force acts in the direction opposite to the

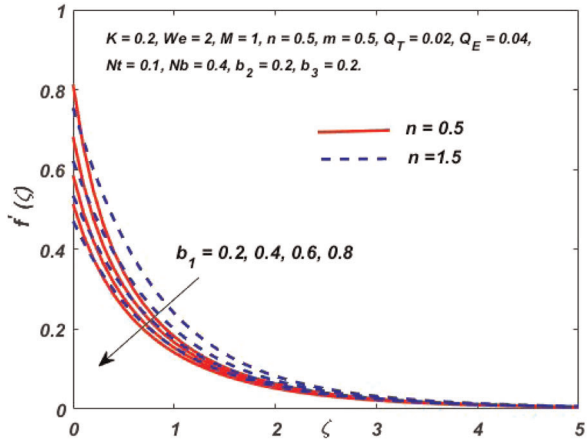

FIGURE 2 $f''(\zeta)$ for differing b_1 values [Color figure can be viewed at wileyonlinelibrary.com]

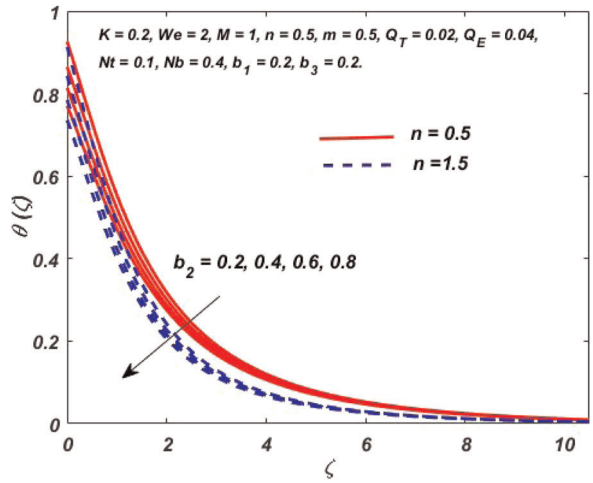

FIGURE 3 $\theta(\zeta)$ for differing b_2 values [Color figure can be viewed at wileyonlinelibrary.com]

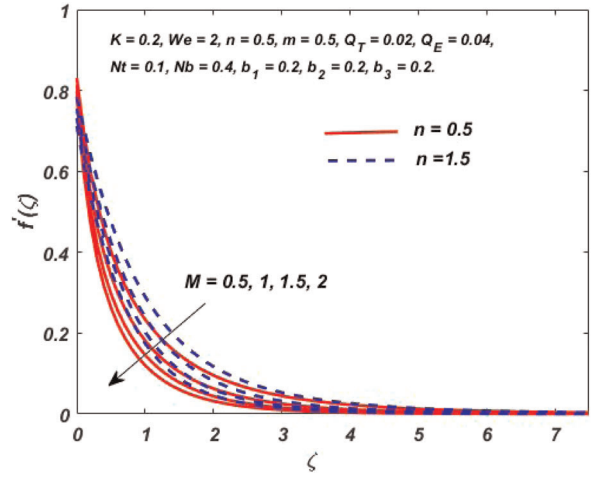

FIGURE 4 $f''(\zeta)$ for differing M values [Color figure can be viewed at wileyonlinelibrary.com]

fluid flow which retards the velocity of both fluids. An increase in *We* escalates the relaxation time of Carreau nanofluid and the fluid thickness grows, which implies that the velocity profile of shear-thinning fluid reduces whereas $f''(\zeta)$ enhances in the case of shear-thickening fluid (shown in Figure 5).

Figure 6 depicts the effect of *We* on $\theta(\zeta)$. The opposite nature is observed on $\theta(\zeta)$ for shear thinning and thickening fluid. Variation in $\theta(\zeta)$ concerning K is described in Figure 7. Physically, an increase in K reduces the cylinder's radius and surface area associated with the fluid which declines the heat transfer rates and hence $\theta(\zeta)$ rises. Figure 8 elucidates the consequence of *Nb* on $\theta(\zeta)$. An increase in *Nb* promotes the random motion of nanoparticles, which enhances the temperature profile. Growing *Nt* values causes the hot fluid particles to move toward the cold region increasing $\theta(\zeta)$ (illustrated in Figure 9).

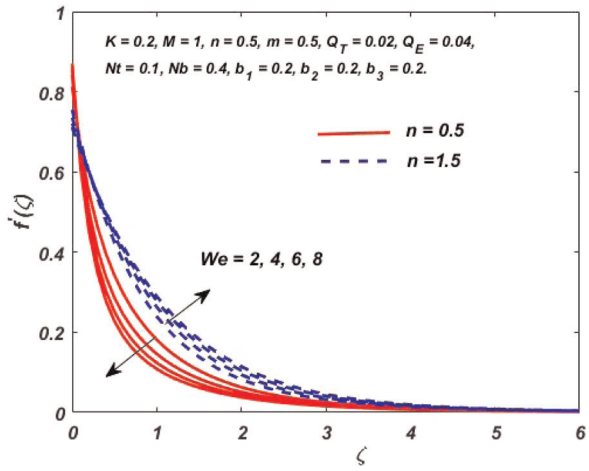

FIGURE 5 $f''(\zeta)$ for differing *We* values [Color figure can be viewed at wileyonlinelibrary.com]

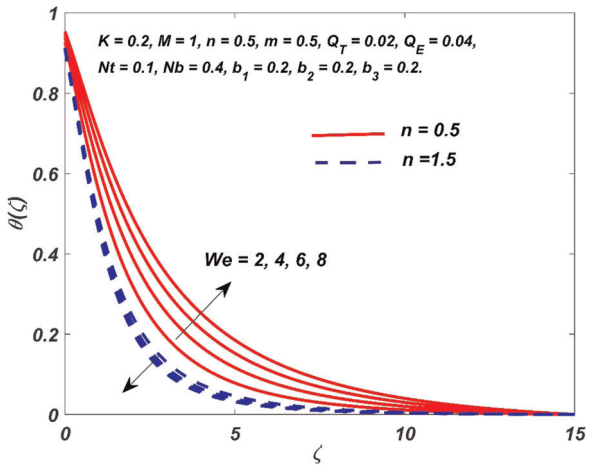

FIGURE 6 $\theta(\zeta)$ for differing *We* values [Color figure can be viewed at wileyonlinelibrary.com]

Figures 10 and 11 describe the variation of $\phi(\zeta)$ due to a rise in Nb and Nt, respectively. An increase in Nb reduces the concentration profile, whereas an increase in Nt increases $\phi(\zeta)$. Figures 12 and 13 illustrate the variation in $\theta(\zeta)$ with increasing Q_T and Q_E values. Both parameters enhance $\theta(\zeta)$. It is also noted that the temperature profile due to variation in Q_E has faster convergence than the temperature profile due to varying Q_T.

The simultaneous impact of differing parameters on $Nu(Re_x)^{\frac{-1}{2}}$ is studied using surface plots, which have been graphed in Figures 14–16. The (A) part analyzes the effects in the case of shear thinning fluids while (B) part examines the effects for shear thickening fluids. The impact of Nt and Nb on the heat transfer rate is described in Figure 14A,B with $K = 0.2$, $We = 2$, $M = 1$, $m = 0.5$, $Q_E = 0.04$, $Q_T = 0.02$ and $b_1 = b_2 = b_3 = 0.2$. $Nu(Re_x)^{\frac{-1}{2}}$ diminishes for greater values of Nb and Nt in both cases ($n = 0.5$ and $n = 1.5$). $Nu(Re_x)^{\frac{-1}{2}}$ is elevated with lower Q_T and Q_E values, as shown in Figure 15A,B with $K = 0.2$, $We = 2$, $M = 1$, $m = 0.5$, $Nb = 0.4$, $Nt = 0.1$ and $b_1 = b_2 = b_3 = 0.2$. The parallel

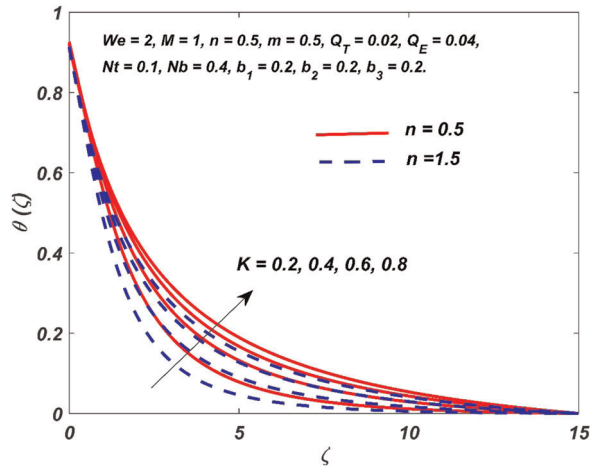

FIGURE 7 $\theta(\zeta)$ for differing K values [Color figure can be viewed at wileyonlinelibrary.com]

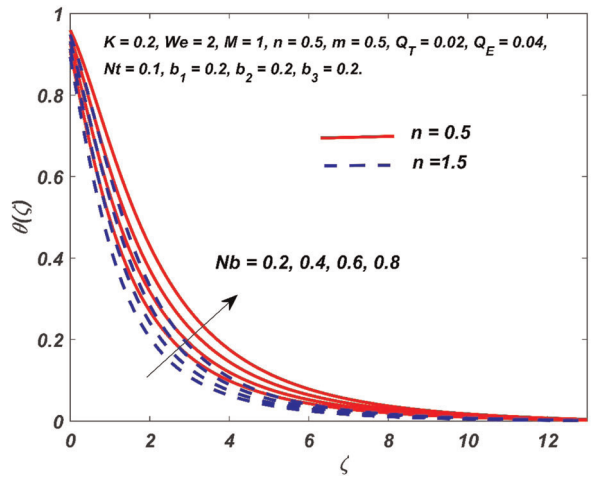

FIGURE 8 $\theta(\zeta)$ for differing Nb values [Color figure can be viewed at wileyonlinelibrary.com]

effect of b_2 and K on the heat transfer coefficient with $We = 2, M = 1, m = 0.5$, $Q_E = 0.04, Q_T = 0.02, Nb = 0.4, Nt = 0.1$ and $b_1 = b_3 = 0.2$ is explained in Figure 16A,B. A rise in K values enhances $Nu\,(Re_x)^{\frac{-1}{2}}$, whereas the heat transfer rate diminishes due to high thermal slip values. Hence, it can be concluded that $Nu\,(Re_x)^{\frac{-1}{2}}$ is directly proportional to K and inversely proportional to Nt, Nb, Q_T, Q_E, and b_2.

The consequence of different parameters on the Sherwood number and drag coefficient when $n = 0.5$ and $n = 1.5$ is described in Tables 3 and 4. Increment/decrement rate indicates the percentage change in the current value with respect to the previous value (preceding entry in the table). A positive sign denotes an increment while a negative sign indicates a decrement.

From Table 3, it is understood that $-\frac{1}{2}Cf\,(Re_x)^{\frac{1}{2}}${for both cases} increases with an increase in K and M values and decreases for increasing values of b_1. It is also seen that We has a negative

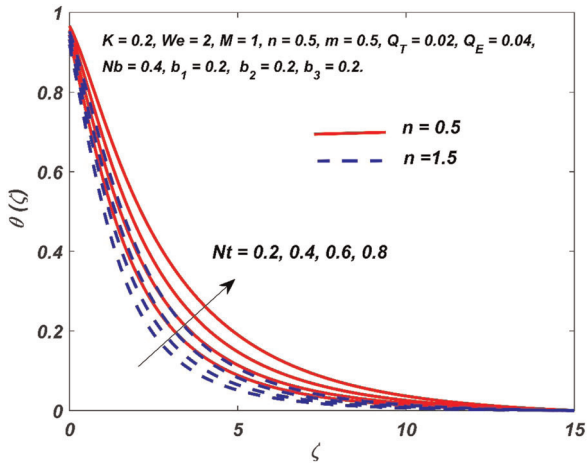

FIGURE 9 $\theta(\zeta)$ for differing *Nt* values [Color figure can be viewed at wileyonlinelibrary.com]

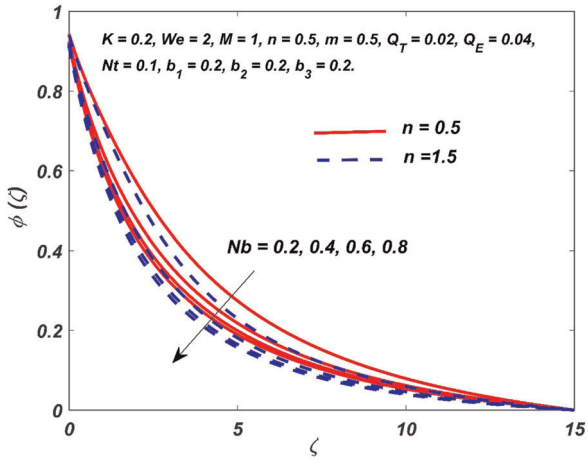

FIGURE 10 $\phi(\zeta)$ for differing *Nb* values [Color figure can be viewed at wileyonlinelibrary.com]

response on $-\frac{1}{2}Cf\,(Re_x)^{\frac{1}{2}}$ (when $n = 0.5$) and it is also seen that the result is reversed for $-\frac{1}{2}Cf\,(Re_x)^{\frac{1}{2}}$ (when $n = 1.5$). From Table 4, it is understood that K and Nb enhance and Nt and b_3 diminish the mass transfer rate.

The nature of variation in Sherwood number and skin friction coefficients due to different parameters has been quantified in Tables 3 and 4 using the slope of linear regression. A positive slope implies that the corresponding parameter enhances the Sherwood number/drag coefficient. The magnitude of slope represents the rate of increase/decrease of drag coefficient/Sherwood number per unit value of the corresponding parameters.

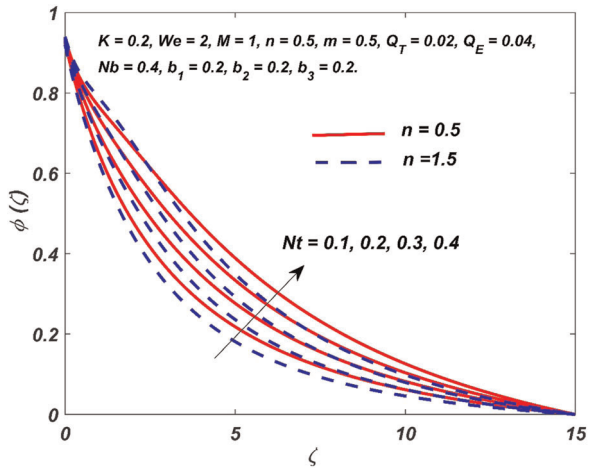

FIGURE 11 $\phi(\zeta)$ for differing Nt values [Color figure can be viewed at wileyonlinelibrary.com]

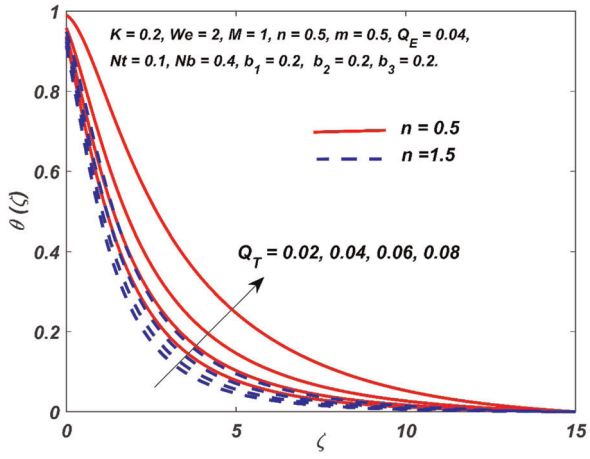

FIGURE 12 $\theta(\zeta)$ for differing Q_T values [Color figure can be viewed at wileyonlinelibrary.com]

4.1 | Statistical analysis

4.1.1 | Correlation and probable error

A statistical technique that helps in predicting the nature and quantity of the relationship between two variables is known as the correlation coefficient ($\mathfrak{r}$). The nature of the relationship is elucidated using sign of $\mathfrak{r}$ and its magnitude predicts the quantity of relationship. The nature of the relationship is identified as positive or negative based on the relation. A positive value in $\mathfrak{r}$ reflects that an increase in one variable correspondingly increases the other variable and the reverse nature is observed for a negative $\mathfrak{r}$ value. The probable error (PE) guarantees the

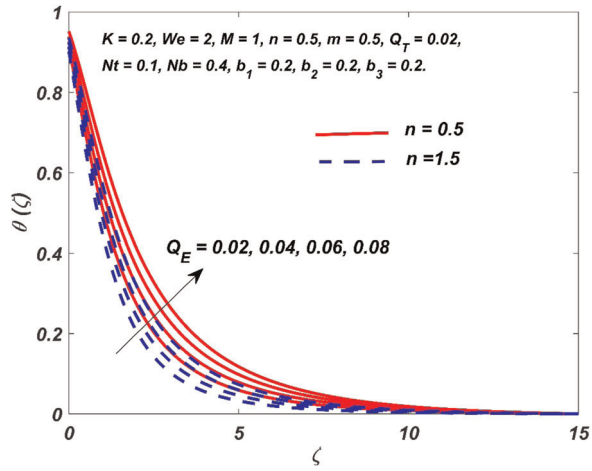

FIGURE 13 $\theta(\zeta)$ for differing Q_E values [Color figure can be viewed at wileyonlinelibrary.com]

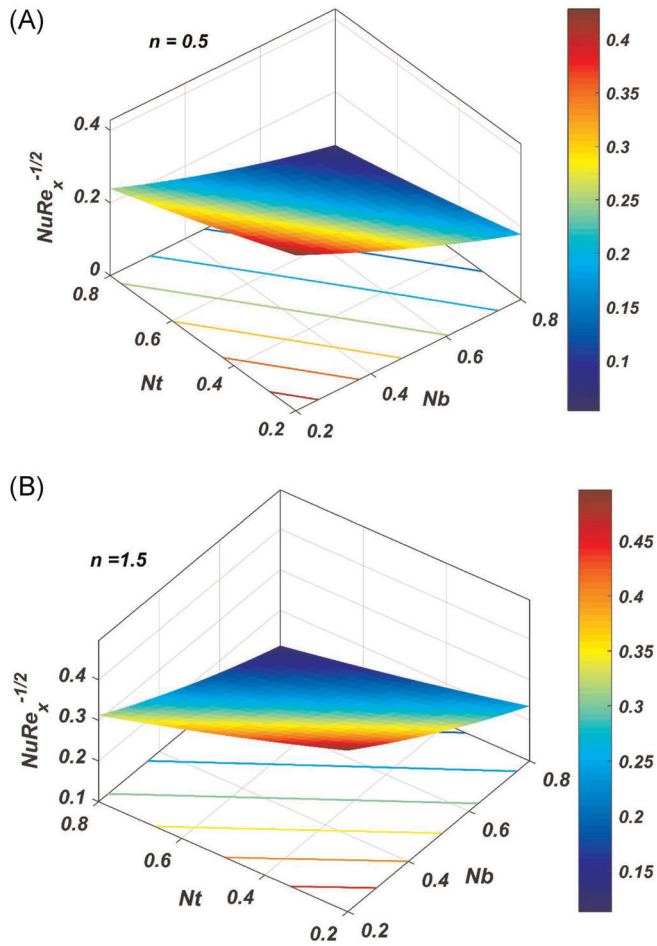

FIGURE 14 (A) Parallel effect of Nb and Nt on $Nu(Re_x)^{\frac{-1}{2}}$ when $n = 0.5$. (B) Parallel effect of Nb and Nt on $Nu(Re_x)^{\frac{-1}{2}}$ when $n = 1.5$ [Color figure can be viewed at wileyonlinelibrary.com]

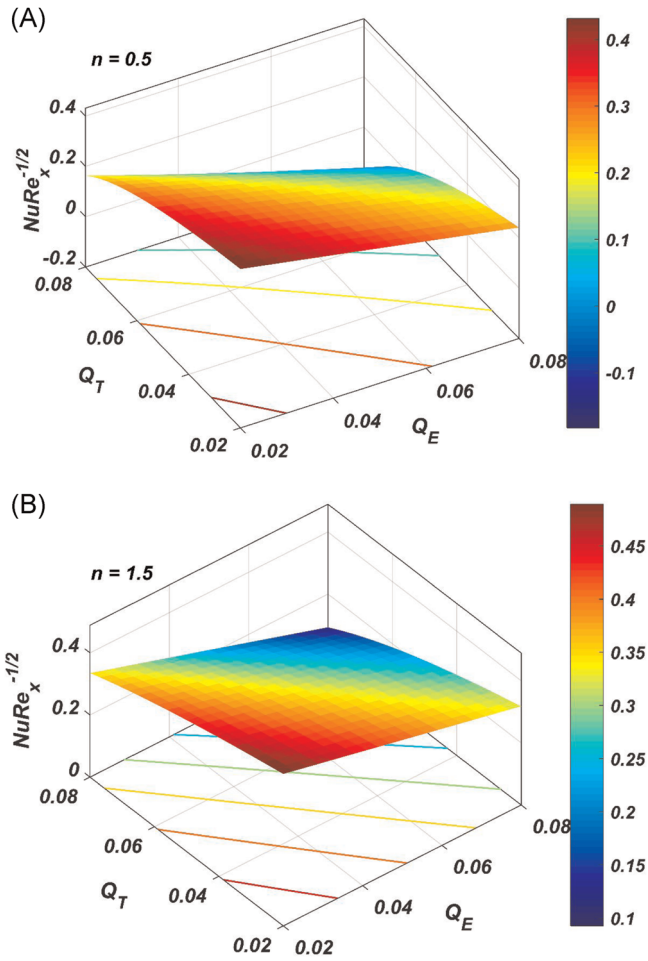

FIGURE 15 (A) Parallel effect of Q_T and Q_E on $Nu(Re_x)^{\frac{-1}{2}}$ when $n = 0.5$. (B) Parallel effect of Q_T and Q_E on $Nu(Re_x)^{\frac{-1}{2}}$ when $n = 1.5$ [Color figure can be viewed at wileyonlinelibrary.com]

reliability of $\mathfrak{r}$ and correlation is ought to be important (see Fisher[33]) when $|\frac{\mathfrak{r}}{\mathrm{PE}}| > 6$; where ϵ denotes the number of observations and $\mathrm{PE} = (\frac{1-\mathfrak{r}^2}{\sqrt{\epsilon}})0.6745$.

It is evident from Table 5 that b_1, b_2, M, Nb, Nt, Q_T, and Q_E are negatively correlated while K exhibits a positive correlation with $Nu(Re_x)^{\frac{-1}{2}}\{\text{both cases}\}$. It is also noted that We shows a differing nature on the heat transfer rate, that is, $\mathfrak{r}$ is positive in case of $Nu(Re_x)^{\frac{-1}{2}}\{\mathrm{n} = 1.5\}$ and negative for $Nu(Re_x)^{\frac{-1}{2}}\{0.5\}$. From $|\frac{\mathfrak{r}}{\mathrm{PE}}|$ values, it can be concluded that all the parameters of $Nu(Re_x)^{\frac{-1}{2}}\{\text{both cases}\}$ are significant.

4.1.2 | Regression analysis

The multiple linear regression model of heat transfer rate (for $n = 0.5$ and 1.5) is estimated using 45 set of values within the range [0.2,0.8] for b_1, b_2, N_b, K, and Nt, [0.02,0.08] for Q_T and Q_E, [0.5,2] for M, and [2,8] for We.

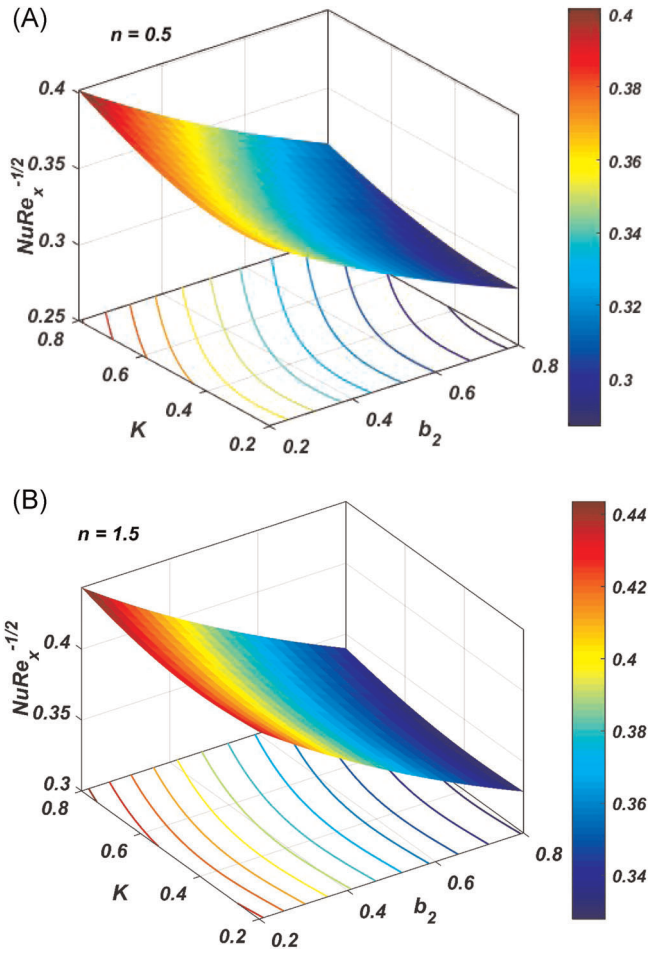

FIGURE 16 (A) Parallel effect of b_2 and K on $Nu(Re_x)^{\frac{-1}{2}}$ when $n = 0.5$. (B) Parallel effect of b_2 and K on $Nu(Re_x)^{\frac{-1}{2}}$ when $n = 1.5$ [Color figure can be viewed at wileyonlinelibrary.com]

The estimated model is given by:

$$Nu_{\text{est}}(n) = c + a_M M + a_{We} We + a_K K + a_{Nb} Nb + a_{Nt} Nt + a_{b_1} b_1 + a_{b_2} b_2 + a_{Q_T} Q_T + a_{Q_E} Q_E,$$

where $c, a_{b_1}, a_{b_2}, a_M, a_{We}, a_K, a_{Nb}, a_{Nt}, a_{Q_T}$, and a_{Q_E} are the estimated regression coefficients. Nusselt number is estimated individually for $n = 0.5$ and $n = 1.5$ with the aid of MATLAB software. The estimated regression models are:

$$Nu_{\text{est}}(0.5) = 1.03641 - 0.26072b_1 - 0.14210b_2 - 0.12386M - 0.02418We + 0.04218K - 0.42863Nb - 0.29557Nt - 4.69465Q_T - 3.20600Q_E,$$

TABLE 3 Variation in $-\frac{1}{2}Cf\,(Re_x)^{\frac{1}{2}}\{\text{at } \zeta = 0\}$ when $K = 0.2$, $We = 2$, $M = 1$, $m = 0.5$, $Q_T = 0.02$, $Q_E = 0.04$, $Nt = 0.1$, $Nb = 0.4$, $b_1 = 0.2$, $b_2 = 0.2$, and $b_3 = 0.2$

				$-\frac{1}{2}Cf\,(Re_x)^{\frac{1}{2}}$		Increment/decrement (%)	
We	***K***	***M***	***b_1***	***n* = 0.5**	***n* = 1.5**	***n* = 0.5**	***n* = 1.5**
2				0.934540	1.225294		
4				0.789978	1.323258	−15.469	7.995
6				0.705486	1.391796	−10.695	5.180
8				0.648771	1.444318	−8.039	3.774
Slope				**−0.047090**	**0.036280**		
	0.2			0.934540	1.225294		
	0.4			0.960097	1.295690	2.735	5.745
	0.6			0.984375	1.361064	2.529	5.045
	0.8			1.007556	1.422289	2.355	4.498
Slope				**0.121664**	**0.328178**		
		0.5		0.845765	1.082917		
		1		0.934540	1.225294	10.496	13.148
		1.5		1.006190	1.342749	7.667	9.586
		2		1.066699	1.443231	6.014	7.483
Slope				**0.146891**	**0.239679**		
			0.2	0.934540	1.225294		
			0.4	0.795551	0.944656	−14.872	−22.904
			0.6	0.690287	0.775479	−13.232	−17.909
			0.8	0.608344	0.660741	−11.871	−14.796
Slope				**−0.541925**	**−0.931419**		

$$Nu_{\text{est}}(1.5) = 0.99305 - 0.35222b_1 - 0.17913b_2 - 0.08699M + 0.00446We + 0.01121K - 0.44799Nb - 0.28786Nt - 2.79750Q_T - 2.86966Q_E.$$

The estimated regression coefficients are significant; as all p values <.05. The accuracy of estimated regression models is described in Figures 17 and 18. It is understood that b_1, b_2, Nb, Nt, Q_T, Q_E, and M have a negative response on the estimated Nu {both cases}. The estimated regression model predicts that the corresponding parameter induces a decreasing effect on Nu meaning that Nu decreases upon increasing parameter values. An increase in K enhances the heat transfer coefficient {for both cases}. The reverse nature is observed due to increasing values of We for $n = 0.5$ and $n = 1.5$. These results are in perfect synchronization with the results discussed in Table 5.

TABLE 4 Variation in $Sh(Re_x)^{-\frac{1}{2}}\{\text{at } \zeta = 0\}$ when $K = 0.2$, $We = 2$, $M = 1$, $m = 0.5$, $Q_T = 0.02$, $Nt = 0.1$ $Q_E = 0.04$, $Nb = 0.4$, $b_i = 0.2$, $b_2 = 0.2$, and $b_3 = 0.2$

				$Sh\,(Re_x)^{-\frac{1}{2}}$		Increment/decrement (%)	
K	Nt	Nb	b_3	$n = 0.5$	$n = 1.5$	$n = 0.5$	$n = 1.5$
0.2				0.371478	0.396258		
0.4				0.459318	0.472917	23.646	19.346
0.6				0.541304	0.549809	17.849	16.259
0.8				0.616713	0.622549	13.931	13.230
Slope				**0.408845**	**0.377883**		
	0.1			0.371478	0.396258		
	0.2			0.339432	0.352109	−8.627	−11.142
	0.3			0.320597	0.320201	−5.549	−9.062
	0.4			0.314358	0.299672	−1.946	−6.411
Slope				**−0.190197**	**−0.321665**		
		0.2		0.283820	0.296854		
		0.4		0.371478	0.396258	30.885	33.486
		0.6		0.399384	0.428064	7.512	8.027
		0.8		0.412213	0.442835	3.212	3.451
Slope				**0.206541**	**0.234875**		
			0.2	0.371478	0.396258		
			0.4	0.340335	0.360624	−8.384	−8.993
			0.6	0.313986	0.330844	−7.742	−8.258
			0.8	0.291408	0.305591	−7.191	−7.633
Slope				**−0.133281**	**−0.150891**		

TABLE 5 Probable error (PE) and correlation coefficient ($\mathfrak{r}$) of $Nu\,(Re_x)^{\frac{-1}{2}}$

	$Nu\,(Re_x)^{\frac{-1}{2}}(n = 0.5)$			$Nu\,(Re_x)^{\frac{-1}{2}}(n = 1.5)$		
Parameter	$\mathfrak{r}$	PE	$\left\lvert\frac{\mathfrak{r}}{PE}\right\rvert$	$\mathfrak{r}$	PE	$\left\lvert\frac{\mathfrak{r}}{PE}\right\rvert$
Q_E	−1.00000	0.00000	2350568.48	−1.00000	0.00000	2572632.69
b_1	−0.99878	0.00073	1361.92	−0.99527	0.00284	349.98
b_2	−0.99756	0.00147	678.85	−0.99705	0.00178	560.30
M	−0.99953	0.00028	3516.14	−0.99971	0.00017	5789.53
We	−0.99382	0.00372	267.47	0.96969	0.01801	53.85
K	0.93349	0.03879	24.06	0.99667	0.00200	497.15
Nb	−0.99886	0.00069	1453.69	−0.99903	0.00058	1712.46
Nt	−0.99948	0.00031	3183.46	−0.99918	0.00050	2012.09
Q_T	−0.97908	0.01249	78.41	−0.99531	0.00282	352.67

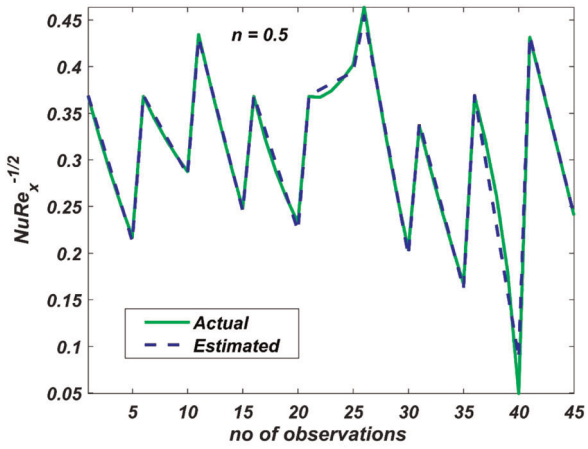

FIGURE 17 Estimated versus actual $Nu(Re_x)^{\frac{-1}{2}}$ when $n = 0.5$ [Color figure can be viewed at wileyonlinelibrary.com]

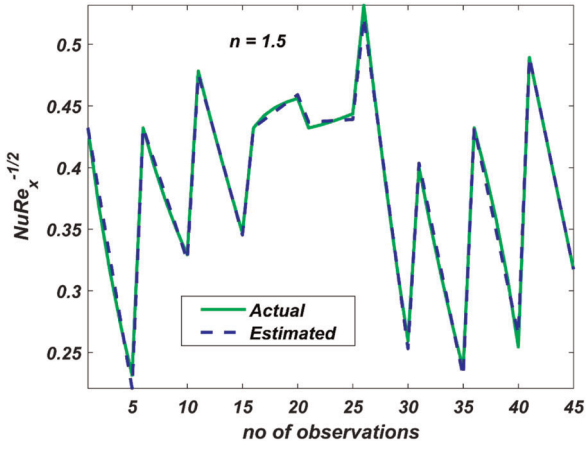

FIGURE 18 Estimated versus actual $Nu(Re_x)^{\frac{-1}{2}}$ when $n = 1.5$ [Color figure can be viewed at wileyonlinelibrary.com]

5 | CONCLUDING REMARKS

The key results of the current study are listed below.

- Hartmann number has a destructive effect on the velocity profile.
- ESHS and LHS parameters exhibit a constructive behavior on the temperature profile.
- Slip effect decreases the velocity and temperature profiles.
- Weissenberg number exhibits a differing nature on the velocity profile based on the nature of fluid; the velocity is reduced when $n < 1$ and increased when $n > 1$.

- Velocity slip increases the drag coefficient whereas the Hartmann number decreases the drag coefficient.
- Heat transfer rate lowers with ESHS, LHS, and temperature slip parameters.
- Mass transfer rate is inversely proportional to the concentration slip parameter.
- Nusselt number has been faultlessly estimated using multiple linear regression.

NOMENCLATURE

u, v	velocity components, m/s
T	fluid temperature, K
C	fluid concentration, mol/kg
a	reference velocity, m/s
l	characteristic length, m
R	Radius of the cylinder, m
x, r	Cylindrical coordinates
T_W	fluid temperature near the wall, K
T_∞	ambient fluid temperature, K
C_W	nanoparticle concentration near the wall, mol/kg
C_∞	ambient nanoparticle concentration, mol/kg
D_T	thermodiffusion coefficient, m^2/s
D_B	Brownian diffusion coefficient, m^2/s
ρC	heat capacity of the fluid, $J/m^3/K$
k_f	fluid's thermal conductivity, W/m/K
We	Weissenberg number
Nt	thermophoresis parameter
Nb	Brownian motion parameter
M	Hartmann number
Sc	Schmidt number
B_0	strength of magnetic field
Pr	Prandtl number
N_i	Slip factor; $i = 1,2,3$
K	curvature parameter
Re_x	local Reynolds number
n	power-law index
m	exponential index
q_T, q_E	heat source coefficients
Q_T	linear heat source
b_i	slip parameters, $i = 1,2,3$
Q_E	exponential space-based heat source

GREEK SYMBOLS

σ	electrical conductivity, s/m
ρ	density, kg/m^3
θ	nondimensional temperature
α	thermal diffusivity, m^2/s
ϕ	dimensionless concentration
ν	kinematic viscosity, m^2/s

Γ time material constant, *s*
ζ dimensionless variable

SUBSCRIPTS

f fluid
p nanoparticle
W condition at the wall

ORCID

Sujesh Areekara http://orcid.org/0000-0001-7860-8268
Alphonsa Mathew http://orcid.org/0000-0002-3810-4484

REFERENCES

1. Shaiq S, Maraj EN, Iqbal Z. A comparative analysis of shape factor and thermophysical properties of electrically conducting nanofluids TiO2−EG and Cu−EG towards stretching cylinder. *Chaos, Solitons Fractals*. 2019;118:290-299. https://doi.org/10.1016/j.chaos.2018.11.032
2. Shojaei A, Amiri AJ, Ardahaie SS, Hosseinzadeh K, Ganji DD. Hydrothermal analysis of non-Newtonian second grade fluid flow on radiative stretching cylinder with Soret and Dufour effects. *Case Stud Therm Eng*. 2019;13:100384. https://doi.org/10.1016/j.csite.2018.100384
3. Hussain Z, Hayat T, Alsaedi A, Ahmed B. Darcy Forhheimer aspects for CNTs nanofluid past a stretching cylinder; using Keller box method. *Results Phys*. 2018;11:801-816. https://doi.org/10.1016/j.rinp.2018.09.029
4. De P. Soret-Dufour effects on unsteady flow of convective Eyring-Powell magneto nanofluids over a semi-infinite vertical plate. *Bionanoscience*. 2019;9:7-12. https://doi.org/10.1007/s12668-018-0583-7
5. Reddy SRR, Bala Anki Reddy P, Rashad AM. Activation energy impact on chemically reacting Eyring–Powell nanofluid flow over a stretching cylinder. *Arab J Sci Eng*. 2020;45:5227-5242. https://doi.org/10.1007/s13369-020-04379-9
6. De P. Impact of dual solutions on nanofluid containing motile gyrotactic micro-organisms with thermal radiation. *Bionanoscience*. 2019;9:13-20. https://doi.org/10.1007/s12668-018-0584-6
7. Roşca NC, Roşca AV, Pop I, Merkin JH. Nanofluid flow by a permeable stretching/shrinking cylinder. *Heat Mass Transfer*. 2020;56:547-557. https://doi.org/10.1007/s00231-019-02730-x
8. De P, Gorji MR. Activation energy and binary chemical reaction on unsteady MHD Williamson nanofluid containing motile gyrotactic micro-organisms. *Heat Transfer*. 2020;49:3030-3043. https://doi.org/10.1002/htj.21759
9. Zeeshan A, Maskeen MM, Mehmood OU. Hydromagnetic nanofluid flow past a stretching cylinder embedded in non-Darcian Forchheimer porous media. *Neural Comput Appl*. 2018;30:3479-3489. https://doi.org/10.1007/s00521-017-2934-7
10. Eid MR, Mahny KL, Dar A, Muhammad T. Numerical study for Carreau nanofluid flow over a convectively heated nonlinear stretching surface with chemically reactive species. *Phys A Stat Mech Its Appl*. 2020;540:123063. https://doi.org/10.1016/j.physa.2019.123063
11. Khan I, Ullah S, Malik MY, Hussain A. Numerical analysis of MHD Carreau fluid flow over a stretching cylinder with homogenous-heterogeneous reactions. *Results Phys*. 2018;9:1141-1147. https://doi.org/10.1016/j.rinp.2018.04.022
12. Salahuddin T, Hussain A, Malik MY, Awais M, Khan M. Carreau nanofluid impinging over a stretching cylinder with generalized slip effects: using finite difference scheme. *Results Phys*. 2017;7:3090-3099. https://doi.org/10.1016/j.rinp.2017.07.036
13. Gholinia M, Armin M, Ranjbar AA, Ganji DD. Numerical thermal study on CNTs/C2H6O2–H2O hybrid base nanofluid upon a porous stretching cylinder under impact of magnetic source. *Case Stud Therm Eng*. 2019;14:100490. https://doi.org/10.1016/j.csite.2019.100490

14. Bilal M, Sagheer M, Hussain S. Numerical study of magnetohydrodynamics and thermal radiation on Williamson nanofluid flow over a stretching cylinder with variable thermal conductivity. *Alexandr Eng J*. 2018;57:3281-3289. https://doi.org/10.1016/j.aej.2017.12.006
15. Sohail M, Naz R. Modified heat and mass transmission models in the magnetohydrodynamic flow of Sutterby nanofluid in stretching cylinder. *Phys A Stat Mech Its Appl*. 2020;549:124088. https://doi.org/10.1016/j.physa.2019.124088
16. Vinita V, Poply V. Impact of outer velocity MHD slip flow and heat transfer of nanofluid past a stretching cylinder. *Mater Today Proc*. 2020;26:3429-3435. https://doi.org/10.1016/j.matpr.2019.11.304
17. Ogunseye HA, Sibanda P, Mondal H. MHD mixed convective stagnation-point flow of Eyring-Powell nanofluid over stretching cylinder with thermal slip conditions. *J Cent South Univ*. 2019;26:1172-1183. https://doi.org/10.1007/s11771-019-4079-6
18. Mishra A, Kumar M. Velocity and thermal slip effects on MHD nanofluid flow past a stretching cylinder with viscous dissipation and Joule heating. *SN Appl Sci*. 2020;2:1350. https://doi.org/10.1007/s42452-020-3156-7
19. Usman M, Soomro FA, Ul Haq R, Wang W, Defterli O. Thermal and velocity slip effects on Casson nanofluid flow over an inclined permeable stretching cylinder via collocation method. *Int J Heat Mass Transfer*. 2018;122:1255-1263. https://doi.org/10.1016/j.ijheatmasstransfer.2018.02.045
20. Ahmed A, Khan M, Hafeez A, Ahmed J. Thermal analysis in unsteady radiative Maxwell nanofluid flow subject to heat source/sink. *Appl Nanosci*. 2020;10:5489-5497. https://doi.org/10.1007/s13204-020-01431-w
21. Ali M, Shahzad M, Sultan F, Azeem Khan W. Numerical analysis of chemical reaction and non - linear radiation for magneto-cross nanofluid over a stretching cylinder. *Appl Nanosci*. 2020;10:3259-3267. https://doi.org/10.1007/s13204-020-01385-z
22. Gireesha BJ, Nagaraja B, Sindhu S, Sowmya G. Consequence of exponential heat generation on non-Darcy-Forchheimer flow of water based carbon nanotubes driven by a curved stretching sheet. *Appl Math Mech—Engl Ed*. 2020;41:1723-1734. https://doi.org/10.1007/s10483-020-2647-7
23. Mahanthesh B, Shashikumar NS, Lorenzini G. Heat transfer enhancement due to nanoparticles, magnetic field, thermal and exponential space - dependent heat source aspects in nanoliquid flow past a stretchable spinning disk. *J Therm Anal Calorim*. 2020. https://doi.org/10.1007/s10973-020-09927-x
24. Mahanthesh B, Shashikumar NS, Gireesha BJ, Animasaun IL. Effectiveness of Hall current and exponential heat source on unsteady heat transport of dusty TiO2 -EO nanoliquid with nonlinear radiative heat. *J Comput Des Eng*. 2019;6:551-561. https://doi.org/10.1016/j.jcde.2019.04.005
25. Nagaraja B, Gireesha BJ. Exponential space-dependent heat generation impact on MHD convective flow of Casson fluid over a curved stretching sheet with chemical reaction. *J Therm Anal Calorim*. 2021;143:4071-4079. https://doi.org/10.1007/s10973-020-09360-0
26. Mahanthesh B, Mackolil J, Shehzad SA. Statistical analysis of stagnation-point heat flow in Williamson fluid with viscous dissipation and exponential heat source effects. *Heat Transfer*. 2020;49:4580-4591. https://doi.org/10.1002/htj.21842
27. Sabu AS, Mathew A, Neethu TS, Anil George K. Statistical Analysis of MHD Convective Ferro-nanofluid Flow through an Inclined channel with Hall current, heat source and Soret effect. *Therm Sci Eng Prog*. 2021;22:100816. https://doi.org/10.1016/j.tsep.2020.100816
28. Mackolil J, Mahanthesh B. Exact and statistical computations of radiated flow of nano and Casson fluids under heat and mass flux conditions. *J Comput Des Eng*. 2019;6:593-605. https://doi.org/10.1016/j.jcde.2019.03.003
29. Sabu AS, Areekara S, Mathew A. Statistical analysis on three-dimensional MHD convective Carreau nanofluid flow due to bilateral nonlinear stretching sheet with heat source and zero mass flux condition. *Heat Transfer*. 2020. https://doi.org/10.1002/htj.22045
30. Mackolil J, Mahanthesh B. Sensitivity analysis of radiative heat transfer in Casson and nano fluids under diffusion-thermo and heat absorption effects. *Eur Phys J Plus*. 2019;134:619. https://doi.org/10.1140/epjp/i2019-12949-6

31. Khan I, Shafquatullah, Malik MY, Hussain A, Khan M. Magnetohydrodynamics Carreau nanofluid flow over an inclined convective heated stretching cylinder with Joule heating. *Results Phys*. 2017;7:4001-4012. https://doi.org/10.1016/j.rinp.2017.10.015
32. Khan W, Pop I. Boundary-layer flow of a nanofluid past a stretching sheet. *Int J Heat Mass Transfer*. 2010; 53:2477-2483. https://doi.org/10.1016/j.ijheatmasstransfer.2010.01.032
33. Fisher R. On the "Probable Error" of a coefficient of correlation deduced from a small sample. *Metron*. 1921;1:1-32. https://ci.nii.ac.jp/naid/10012392243/en/

How to cite this article: Sabu AS, Areekara S, Mathew A. Effects of multislip and distinct heat source on MHD Carreau nanofluid flow past an elongating cylinder using the statistical method. *Heat Transfer*. 2021;1-22. https://doi.org/10.1002/htj.22142